ARTICLES
PUBLISHED ONLINE: 11 JANUARY 2016 | DOI: 10.1038/NCHEM.2431
nature chemistry

Extreme compressibility in $LnFe(CN)_6$ coordination framework materials via molecular gears and torsion springs

Samuel G. Duyker[1,2], Vanessa K. Peterson[2]*, Gordon J. Kearley[2], Andrew J. Studer[2] and Cameron J. Kepert[1]*

The mechanical flexibility of coordination frameworks can lead to a range of highly anomalous structural behaviours. Here, we demonstrate the extreme compressibility of the $LnFe(CN)_6$ frameworks (Ln = Ho, Lu or Y), which reversibly compress by 20% in volume under the relatively low pressure of 1 GPa, one of the largest known pressure responses for any crystalline material. We delineate in detail the mechanism for this high compressibility, where the LnN_6 units act like torsion springs synchronized by rigid $Fe(CN)_6$ units performing the role of gears. The materials also show significant negative linear compressibility via a cam-like effect. The torsional mechanism is fundamentally distinct from the deformation mechanisms prevalent in other flexible solids and relies on competition between locally unstable metal coordination geometries and the constraints of the framework connectivity, a discovery that has implications for the strategic design of new materials with exceptional mechanical properties.

The most compressible crystalline materials currently known derive their extreme properties from the high compressibility of the chemical bonds within their structures. Such a feature is predominant in very simple materials such as alkali metals (for example, caesium and rubidium), which have low valence-electron densities, and noble gases (such as xenon, which is solid below −112 °C), for which only weak dispersion forces exist between the atoms[1–3]. A consequence of this reliance on bonding characteristics to yield extreme compressibilities is that such materials are commonly impractical for functional use due to their high chemical reactivity and/or low melting/sublimation points. An alternative strategy for achieving extreme compressibilities is to target geometric changes within materials that are structurally more complex, in which the application of pressure leads to progressive distortion of the lattice towards a more condensed three-dimensional configuration.

This approach has recently been exploited in coordination frameworks, a class of materials constructed from metal ions interconnected three-dimensionally by molecular linkers. The flexibility inherent in many of these structures gives rise to a range of highly anomalous structural behaviours, such as extreme expansion and contraction in response to the adsorption and desorption of molecular guests[4] and large and even negative framework compressibility[5–12] and thermal expansion[13–19]. Such mechanical behaviours are interesting on a fundamental level as well as being desirable for the next generation of high-pressure components and devices, and arise due to the low energies required to distort the open framework lattices. Folding wine-rack mechanisms are prevalent in a number of flexible frameworks[6,9–11] as well as some molecular solids[20–22], yielding large positive linear compressibility (PLC) along one direction coupled with the unusual phenomenon of negative linear compressibility (NLC), wherein one or more of the other dimensions lengthen under increasing pressure. The net effect of combined PLC and NLC is relatively low volume compressibility in these materials.

Here, we show that combining flexibility with empty void spaces leads to extreme volume and linear compressibility in the lanthanoid hexacyanidoferrate frameworks $LnFe(CN)_6$ (Ln = Ho, Lu, Y). These materials consist of trigonal prismatic Ln^{III} and octahedral Fe^{III} centres connected by cyanide bridges to form a three-dimensional hexagonal porous lattice (Fig. 1a). The trigonal prismatic six-coordinate Ln geometry found in these materials is highly unusual and is generated topotactically upon the thermal removal of coordinated water molecules from the parent hydrated form[23]. This Ln geometry is locally unstable, with the rearrangement of the LnN_6 unit to the octahedral shape favoured by six-coordinate complexes[24] being prevented by the competing preference of the framework cyanide ions to connect linearly. We explore in detail the novel torsional geometric mechanism for the high compressibility in the $LnFe(CN)_6$ materials using a combination of neutron powder diffraction (NPD) and density functional theory (DFT) calculations.

Results and discussion

Structural characterization. NPD measurements were used to determine the pressure dependence of the room-temperature structures of several anhydrous $LnFe(CN)_6$ frameworks, as well as the as-synthesized deuterated hydrate, $LaFe(CN)_6{\cdot}5D_2O$ (Fig. 1b). The anhydrous materials show a brief 'hard' regime, with relatively low compressibility from ambient pressure to 0.15–0.40 GPa, followed by a 'soft' regime during which the materials undergo extreme compression, with up to 25% volume reduction by the relatively low pressure of 1.5 GPa. The compression is accompanied by a change from the original hexagonal $P6_3/mmc$ symmetry to trigonal $P31c$ symmetry, which is allowed to be a continuous transition in renormalization-group theory (ISOTROPY Software Suite, iso.byu.edu). The resolution and pressure spacing of the NPD data may not be sufficient to establish conclusively the continuous nature of the transition, although the distortion energetics discussed below show no discontinuities.

[1]School of Chemistry, The University of Sydney, Sydney, New South Wales 2006, Australia. [2]Australian Nuclear Science and Technology Organisation, Locked Bag 2001, Kirrawee DC, New South Wales 2232, Australia. *e-mail: vanessa.peterson@ansto.gov.au; c.kepert@chem.usyd.edu.au

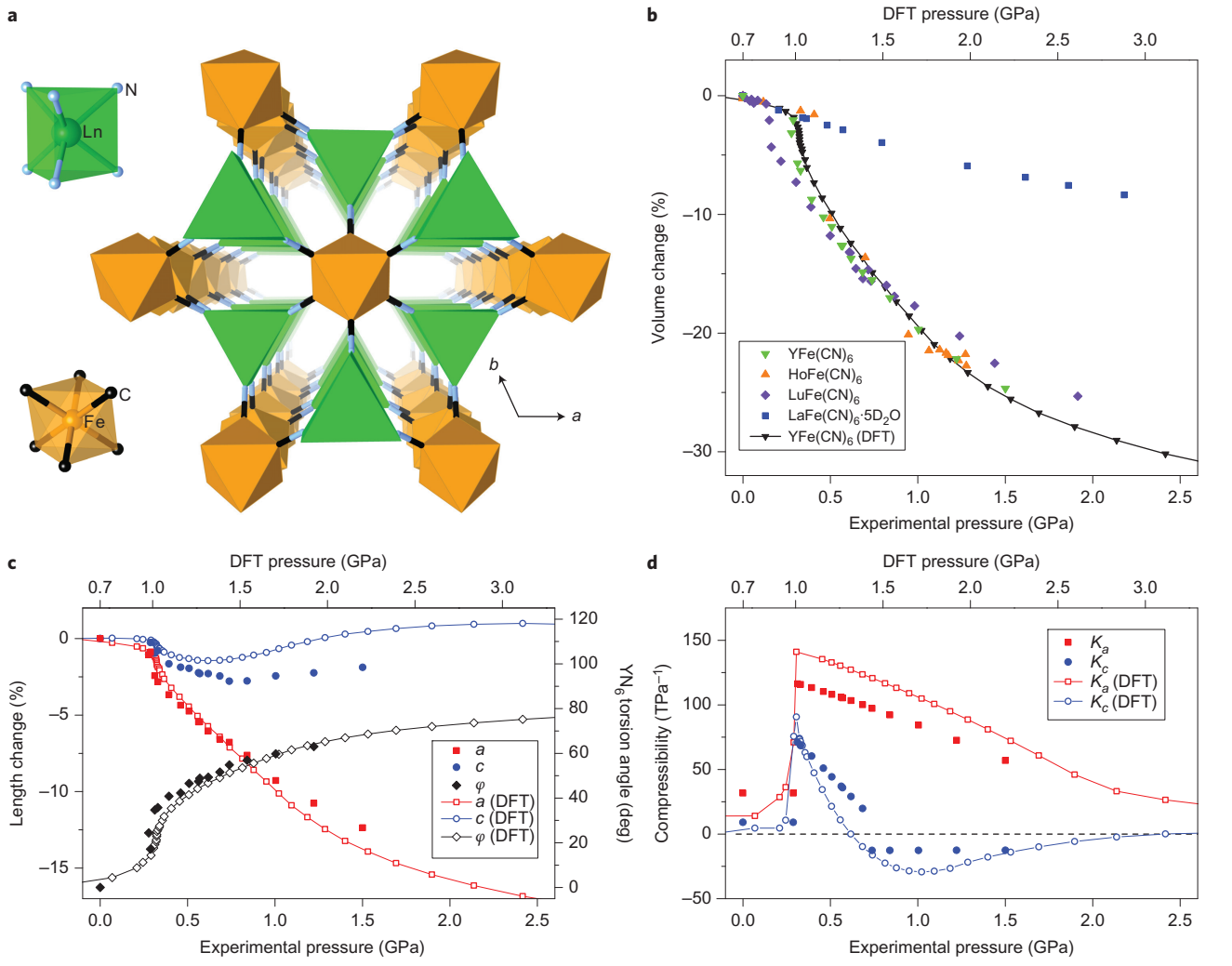

Figure 1 | Structure and pressure-induced behaviour of $LnFe(CN)_6$ frameworks. a, Hexagonal structure of $LnFe(CN)_6$, consisting of alternating LnN_6 trigonal prisms (green) and FeC_6 octahedra (orange). The C (black) and N (blue) atoms of the cyanide bridges are also shown. **b**, Pressure-dependent volume behaviour of anhydrous $LnFe(CN)_6$ (Ln = Y, Ho, Lu) and $LaFe(CN)_6{\cdot}5D_2O$ obtained from NPD, and $YFe(CN)_6$ obtained from DFT calculations. The large volume compressibility of the anhydrous materials is evident. The DFT-derived parameters were found to be shifted by 0.7 GPa relative to the NPD parameters as described in the Methods. **c**, Experimental and DFT-calculated pressure-dependent lattice parameters (a and c) of $YFe(CN)_6$, showing large compression in a, accompanied by an increase in the YN_6 torsion angle φ. The moderate positive compressibility in c is followed by negative compressibility behaviour for $\varphi > 60°$. **d**, Pressure-dependent linear compressibilities (K_a and K_c) of $YFe(CN)_6$, determined from the experimental and calculated lattice parameters.

NPD data collected with progressively decreasing pressure, and at ambient pressure at the conclusion of the experiment, demonstrate the fully elastic nature of the materials (Supplementary Fig. 1).

The bulk modulus B_0, which quantifies resistance to compression, was determined for each material within the hard and soft regimes by fitting Birch–Murnaghan equations of state to the experimental data (Supplementary Fig. 2). The very low B_0 values of 2.72(16) and 2.6(5) GPa for the Y and Lu materials, respectively, under the soft regime are close to those of highly compressible solid polymers such as polystyrene (3–4 GPa)[25]. Among crystalline materials, these values are comparable to those for elemental Cs and Rb (1.7 and 2.3 GPa, respectively)[1,2] and the much lower density frameworks ZIF-4 (2.6 GPa), which amorphizes above 0.35 GPa following a total volume compression of 10% (ref. 8), and MIL-53(Cr) ($B_0 = 2$ GPa over the narrow pressure range 0–0.04 GPa; volume compression 2.7%)[26].

Torsional compression mechanism. In contrast to solid Cs and Rb, which achieve similar volume compression through a reduction in bond distances but no change in lattice geometry, the compression of $YFe(CN)_6$ progresses via a complex mechanism involving dramatic structural distortion. Structure refinements from the NPD data reveal that, under increasing pressure, the YN_6 unit progressively twists away from its original trigonal prismatic geometry (axial torsion angle $\varphi = 0°$, where φ is the N–Y–N angle projected onto the a–b plane as indicated in Fig. 2b), becoming octahedral near 1 GPa ($\varphi = 60°$, Supplementary Fig. 3). *Ab initio* calculations based on DFT, undertaken to explore the pressure-dependent behaviour independently, closely reproduce the experimentally determined lattice parameters and structural deformation, with a constant offset in absolute pressure of 0.7 GPa (Fig. 1b,c; see Methods for details). The calculations show that the YN_6 unit continues to twist at higher pressures such that at a calculated pressure of 2.7 GPa ($\varphi = 74°$) the twist approaches a one-third turn and a return to trigonal prismatic geometry (Fig. 2; also Supplementary Fig. 4 and Supplementary Movie). Twisting of the YN_6 units necessitates bending of the Y–N–C–Fe linkages, which occurs almost exclusively at the N atom. We find that the entire $Fe(CN)_6$ unit is almost completely rigid up to ~3 GPa, above which it begins to flatten along the

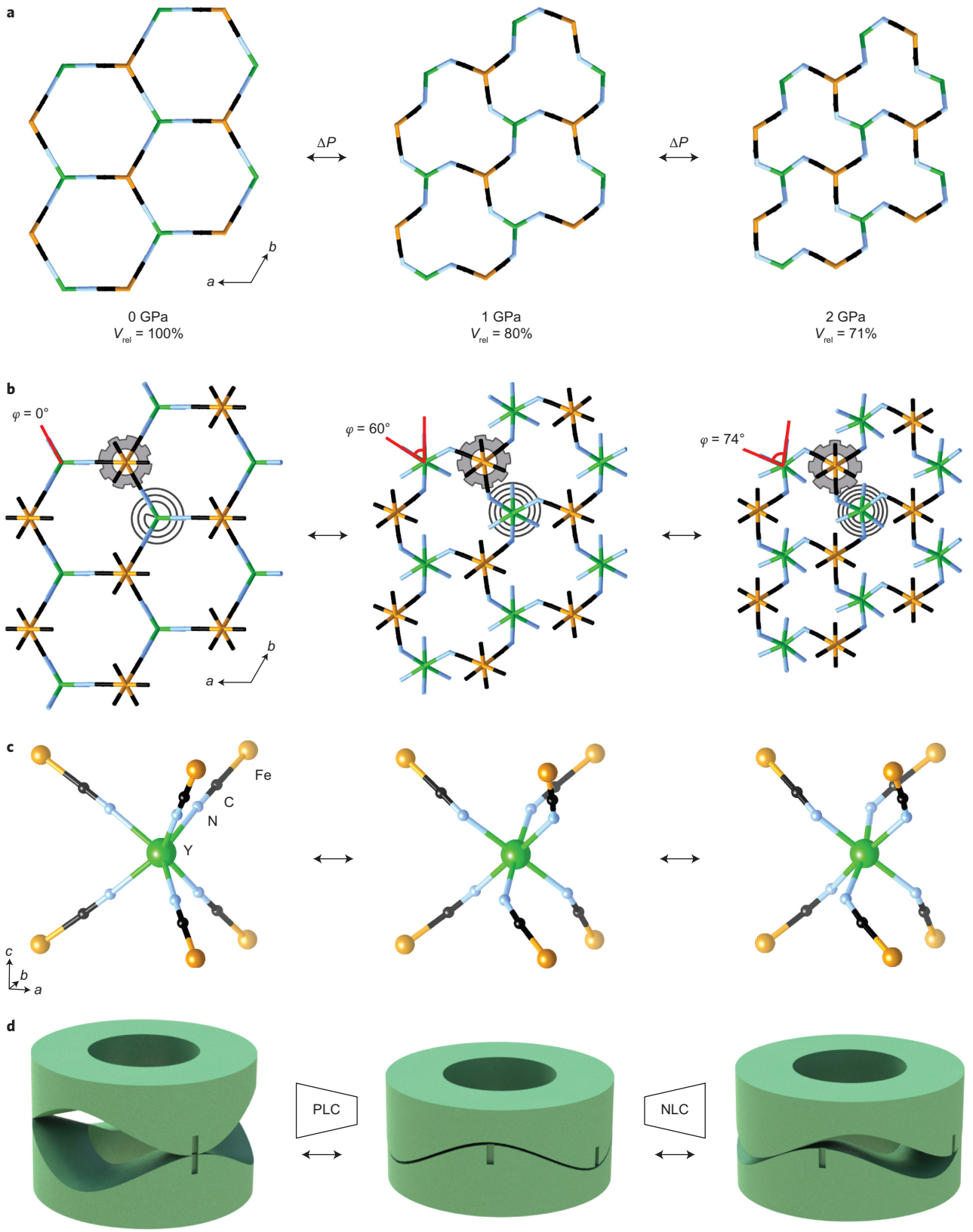

Figure 2 | Spring-and-gear mechanism for compression. a, An atom-thick projection along the *c* axis of the $YFe(CN)_6$ structure, showing the distortion of the structure under pressure from the original hexagonal symmetry to trigonal symmetry. V_{rel} is the volume as a percentage of the ambient-pressure volume. **b**, A thicker projection, showing how the torsion-spring-like YN_6 units twist from trigonal prismatic geometry at ambient pressure (torsion angle, $\varphi = 0°$), to octahedral at 1 GPa ($\varphi = 60°$), and again towards trigonal prismatic at higher pressures ($\varphi = 74°$ at a DFT-calculated pressure of 2.7 GPa, equivalent to 2 GPa experimental pressure). This twisting is accompanied by rotation of the rigid gear-like $Fe(CN)_6$ units. **c**, The local Y coordination geometry at these pressures. Y atoms are shown in green, Fe in orange, C in black and N in blue. **d**, Illustration of the cam-like behaviour of the YN_6 unit, which as it twists gives rise to PLC (contraction with increasing pressure) followed by NLC (expansion with increasing pressure) along the *c* axis.

c axis, as further distortion of the YN_6 unit becomes relatively more difficult. The pressure-induced distortion is analogous to the framework deformation induced by the internal attractive effect of K^+ ions in the $KLnFe^{II}(CN)_6$ anionic framework phases, which possess a similar coiled trigonal structure[27]. The observed ~20% volume compression at 1 GPa is comparable to the 23% reduced volume for $KLaFe(CN)_6$ relative to $LaFe(CN)_6$ at ambient pressure. The distortion is also a static analogue of the vibrational mode identified previously in $LnCo(CN)_6$ whereby the non-rigid LnN_6 prism twists dynamically about its trigonal axis at very low energies[18], with the thermal flexibility that leads to negative thermal expansion here manifested as a mechanical flexibility. In contrast to the anhydrous materials $LnFe(CN)_6$, the hydrated phase $LaFe(CN)_6{\cdot}5D_2O$ cannot readily undergo a Ln twisting deformation due to three water molecules filling a now stable nine-coordinate La coordination sphere and two lattice water molecules occupying the pore space. Instead, this phase compresses via static rotation of its tricapped trigonal prismatic $La(NC)_6(OH_2)_3$ units, in a manner akin to the dynamic rigid-unit mode present in this family of materials[18], to yield a volume compressibility that is greatly reduced although still appreciable ($B_0 = 14.9(13)$ GPa; Supplementary Fig. 5).

The DFT calculations show that the twisting takes place during the hard regime at relatively small applied pressures, indicating that the built-in framework strain may cause the hexagonal symmetry to be formally broken even at ambient pressure. The relatively small rate of volume change with pressure observed within the hard regime of $LnFe(CN)_6$ corresponds to a pressure range in which the Ln–NC–Fe linkage adopts a relatively straight geometry that is resistant to compression; in this regime, angular deformation of the structure yields only minor linear and volumetric changes. Only once this linkage is sufficiently bent does further application of pressure yield a pronounced volumetric change, enabling the rapid decrease in volume seen in the early stage of the soft regime. The compression under the soft regime proceeds similarly for the three materials, with the Y and Ho analogues displaying a slightly greater relative volume reduction at 1 GPa than the Lu analogue; this is attributable to their larger void volumes, which allow the cyanide linkages more room to bend. This trend is supported by the DFT calculations for a range of different Ln analogues (Supplementary Fig. 6), which show an increase in compressibility with increasing Ln ionic radius. These calculations predict that $LaFe(CN)_6$ has two to three times greater compressibility during the soft regime than the Y and Ho analogues, probably as a result of the weaker bonding and more flexible linkages, which is in keeping with the link between Ln size and the magnitude of negative thermal expansion in this series[18]. Experimentally, we observe that $LaFe(CN)_6$ permanently loses crystallinity above ~0.3 GPa, perhaps as a result of its greater flexibility making it difficult to retain long-range order during compression.

Axial compressibilities. A consequence of the axial nature of the torsion-spring-like mechanism is that the behaviour of the $LnFe(CN)_6$ materials is highly anisotropic, with most of the compression occurring in the *a*–*b* plane (Supplementary Fig. 7). These materials display one of the largest sustained linear compressibilities ever reported. For $YFe(CN)_6$ the compressibility along the *a* axis, $K_a = -1/a(da/dP)$ averages 90 TPa^{-1} between 0.4 and 1.5 GPa, and is larger than that of any other crystalline solid, including Cs, over this pressure range (Supplementary Fig. 8). In comparison, the compression along the *c* axis is relatively minor. The maximal 2.8% decrease in *c* from 0 to 0.74 GPa corresponds to the decreasing height (dimension parallel to the *c* axis) of the YN_6 polyhedron as it twists from the 'eclipsed' trigonal prism ($\varphi = 0°$) to the 'staggered' octahedron ($\varphi = 60°$). The experimental data show significant NLC in the *c* lattice parameter above

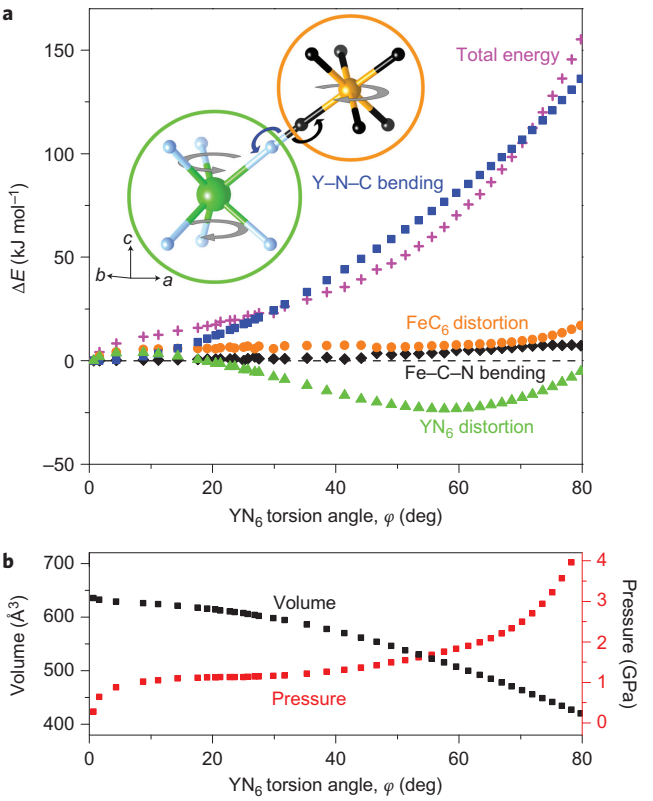

Figure 3 | Energetic origin of the behaviour. a, DFT-calculated energy changes in the structural components of $YFe(CN)_6$ as a function of the YN_6 torsion angle φ. The plots are colour-coded to correspond to the features indicated in the inset. The combination of the energy advantage from twisting the YN_6 geometry (originally trigonal prismatic, $\varphi = 0°$) towards its more favourable octahedral arrangement ($\varphi = 60°$) and the energy penalty of bending the six attached cyanide linkages gives a relatively flat total energy curve as a function of the structural distortion. The total energy increases rapidly once the YN_6 unit begins to distort beyond its most stable configuration. Y atoms are shown in green, Fe in orange, C in black and N in blue. **b**, DFT-calculated unit-cell volume and pressure as a function of φ, highlighting the smooth dependence of the volume on distortion, and the flattening of the pressure profile upon the change from hard to soft regimes at $\varphi = \sim 5°$.

0.74 GPa for $YFe(CN)_6$ and $LuFe(CN)_6$. The DFT calculations for $YFe(CN)_6$ reproduce this NLC effect (Fig. 1c,d), showing that the *c* parameter increases between calculated pressures of 1.3 and 3.1 GPa because the LnN_6 height increases as it continues its twist beyond the octahedral state and towards a second trigonal prismatic geometry. The overall behaviour of the LnN_6 polyhedron is like that of two counter-rotating sinusoidal axial cams (Fig. 2d); this cam-like behaviour is distinct from the established NLC mechanisms[12]. Despite the twist continuing above 3 GPa, the *c* parameter begins to decrease again above this pressure, once even the relatively robust $Fe(CN)_6$ unit begins to yield and flatten under the pressure (Supplementary Fig. 9). The measured NLC is one of the stronger such sustained effects reported so far, with $K_c = -12.7(10)$ TPa^{-1} between 0.74 and 1.5 GPa, which is closely comparable to the value of $-12.0(8)$ TPa^{-1} for $KMn[Ag(CN)_2]_3$ (ref. 9), cf. the larger sustained NLC in MIL-53(Al) (-28 TPa^{-1})[28] and $Zn[Au(CN)_2]_2$ (-42 TPa^{-1})[10].

Energetics of distortion. In considering the general nature of the mechanisms for materials compression, we note first that pronounced mechanical behaviour has relied conventionally on the

presence of a weak interaction, such as that present between atoms in Cs, Rb and Xe (Supplementary Fig. 10) or the metallophilic Au···Au interaction underlying the large PLC and NLC in $Zn[Au(CN)_2]_2$ (ref. 10). The mechanism for extreme compressibility in $LnFe(CN)_6$, in contrast, results from the competition between two relatively strong effects. Here, there is a balance between the significant stored energy in the locally unstable Ln coordination, which is akin to a pre-wound torsion spring, and the opposing force of the Ln–N–C–Fe linkage, which strongly prefers to remain linear. These opposing effects combine to yield a LnN_6 unit that can be likened to a soft spiral torsion spring. This contrasts with the highly rigid $Fe(CN)_6$ unit, which acts like a molecular gear that synchronizes the twists of its neighbouring LnN_6 units within the highly cooperative lattice. An examination of the DFT-calculated energy changes in the individual components of the $YFe(CN)_6$ framework (shown in Fig. 3 as a function of the YN_6 torsion angle, φ) reveals the magnitude of these competing effects. The largest local energy increase lies in the bending of the Y–N–C bond angles, while the greatest local decrease is associated with twisting of the YN_6 unit towards a more locally stable arrangement, with the local energy minimum of the latter occurring at the point where it is an almost perfect octahedron (N–Y–N angles of 87.8°, 92.0°, 92.4° and 179.7°; $\varphi = 59.6°$). In the region of largest volume compressibility, the energy penalty in bending the linkages is offset to a large extent by the energetic advantage of restoring the YN_6 coordination to its most locally stable configuration. Beyond this point, further distortion away from the octahedral geometry results in a local energy increase and the total energy required to further distort and compress the structure increases rapidly. Notably, the energy advantage provided by the YN_6 twisting is approximately proportional to $\cos(3\varphi)$ and is relatively flat at small values of φ (that is, during the hard regime) but decreases rapidly soon thereafter, this being another reason for the hard–soft change in addition to the geometric effect discussed earlier. The energy changes in the FeC_6 fragment and Fe–C–N bond angles are minimal until above 3 GPa, whereupon they begin to distort significantly as they become the relatively softer part of the framework.

Conclusion

Compared with similarly compressible crystals such as Cs, Rb and Xe[1–3], the $LnFe(CN)_6$ frameworks are easier to handle, maintain their structures to higher temperature[18] and are transparent in regions of the visible spectrum, facilitating their potential use in piezo-optical devices such as interferometric pressure sensors[29]. The luminescent properties[30] found in this family of materials are also likely to change upon compression, particularly given the large changes in Ln coordination geometry, providing another possible method of pressure measurement. The challenge in designing analogous structures with even more pronounced thermomechanical behaviours lies in finding a way to increase the energy gain associated with local distortion of the unstable Ln geometry and/or minimize the energy penalty associated with bending of the cyanide linkages, so as to finely balance these competing effects. More broadly, we anticipate that the approach of stabilizing high-energy coordination geometries within framework architectures will enable the development of a great variety of new materials with extreme properties, such as large positive or negative thermal expansion, or even greater compressibility than that described here.

Methods

Sample preparation. As shown in our previous work[27], slow diffusion of equimolar aqueous solutions of Ln^{III} nitrates (Ln = La, Ho, Lu, Y) and $K_3Fe(CN)_6$ yielded red crystals or rust-coloured powders of $LnFe(CN)_6{\cdot}nH_2O$ ($n = 5$ for La; $n = 4$ for Ho, Lu, Y). $LaFe(CN)_6{\cdot}5D_2O$ was prepared in D_2O to reduce the incoherent background contribution to the neutron diffraction data that arises from regular hydrogen. The crystals or powders were ground using a mortar and pestle before further analysis. Anhydrous $LnFe(CN)_6$ samples were prepared by heating the hydrates at 150 °C under vacuum (~10^{-3} mbar) for 12–24 h.

High-pressure NPD. NPD measurements were carried out using WOMBAT[31], the high-intensity neutron powder diffractometer at the OPAL reactor facility, Australian Nuclear Science and Technology Organisation (ANSTO). The powdered sample (~100 mg) was mixed under an Ar atmosphere with NaCl (~50 mg) as an internal pressure standard[32] and Fluorinert FC-70 (perfluorotripentylamine) as a large-molecule non-penetrating pressure medium. The resulting slurry was loaded into a TiZr null matrix alloy sample holder, which was placed in a VX-5 Paris-Edinburgh hydraulic press equipped with boron nitride anvils[33]. Diffraction data were acquired using an area detector that continuously covers 120° with usable data obtained in the angular range $16° < 2\theta < 105°$ acquired over 10–30 min at each pressure with the instrument's oscillating collimator active and 2.411 Å neutrons as determined using a LaB_6 reference (NIST SRM 660b). Due to beamtime constraints, data from the $YFe(CN)_6$ sample returned to ambient pressure from 1.5 GPa were collected at a later time, using a wavelength of 2.415 Å.

Analysis of powder diffraction data. Analysis of the NPD data was carried out using the GSAS[34] and EXPGUI[35] software packages. The background from the sample environment and pressure medium was modelled using a shifted Chebyshev polynomial. Ambient-pressure structures were treated using the original hexagonal $P6_3/mmc$ space group, which is replaced by the trigonal $P\bar{3}1c$ space group (as in $KLnFe(CN)_6$)[27] on application of pressure. Some unreliability in the position of the relatively weakly scattering C atom was encountered, producing unreasonably large Fe–C distances and nonlinear Fe–C–N angles. Our previous theoretical and experimental investigations of these materials have demonstrated that bending of the linkage at the C atom is highly disfavoured[18]. The Fe–C and C–N bond distances were therefore restrained to maintain close to their ambient-pressure values, which reduced the apparent bend in the linkage significantly. The standard uncertainties on values obtained from the refinement software are smaller than the data points in the main and Supplementary figures unless error bars are shown. Refined unit cell and structure parameters are tabulated in Supplementary Tables 4–8. Equation of state fitting utilized PASCal software[36] and is detailed in the Supplementary Methods.

DFT calculations. DFT calculations on the periodic $LnFe(CN)_6$ structures were performed in VASP 5.2.12[37] software with the standard PAW pseudopotentials[38,39], using the PBE[40] GGA functional, with Gaussian smearing of partial orbital occupancies, a plane-wave energy cutoff of 600 eV and a gamma-centred $5 \times 5 \times 5$ K-point mesh. Energy minimizations were performed for a series of steadily reducing fixed unit-cell volumes, with the cell shape and atomic positions allowed to relax. The pressure required to stabilize each of these structures was then extracted from the calculated stress tensor, which allowed delineation of the structure as a function of applied hydrostatic pressure. Supplementary Tables 1 and 2 show listed values of the calculated pressure, unit cell and structure parameters. The calculated pressure for a given volume is 0.7 GPa higher relative to the experimental results. Such a difference, typically on the order of 1 GPa for simple inorganic and small-molecule systems, can arise in DFT calculations when an empirical correction is not used to account for van der Waals forces[41–43]. Seven of the calculations, spread across the P–V curve between 0 and 2 GPa, were repeated with the Grimme DFT-D2 dispersion correction enabled[44], yielding a 0.68 GPa average reduction in the calculated pressure, thus providing evidence of van der Waals interactions as the origin of the discrepancy. A number of pressure-dependent calculations were performed to test agreement with the volume-dependent method, providing very similar results, including within the steepest section of the P–V curve (Supplementary Fig. 11). All-electron DFT energy calculations were carried out on the isolated $Y(NC)_6^{3-}$ and $Fe(CN)_6^{3-}$ fragments of the $YFe(CN)_6$ structure, with the geometries of these fragments extracted from each of the above periodic structures. These calculations were performed using DMol3 v6.0 within Materials Studio[45,46], for the convenience of scripting to automate the structure extraction, with a PBE functional, Fermi treatment of occupancies, an orbital cutoff of 5.6 Å and a fine integration grid. The Supplementary Methods and Supplementary Table 3 show further details of these fragment calculations.

Received 19 June 2015; accepted 26 November 2015; published online 11 January 2016

References

1. Anderson, M. S. & Swenson, C. A. Experimental compressions for sodium, potassium, and rubidium metals to 20 kbar from 4.2 to 300 K. *Phys. Rev. B* **28,** 5395–5418 (1983).
2. Anderson, M. S. & Swenson, C. A. Experimental equations of state for cesium and lithium metals to 20 kbar and the high-pressure behavior of the alkali-metals. *Phys. Rev. B* **31,** 668–680 (1985).
3. Packard, J. R. & Swenson, C. A. An experimental equation of state for solid xenon. *J. Phys. Chem. Solids* **24,** 1405–1418 (1963).
4. Serre, C. *et al.* Role of solvent–host interactions that lead to very large swelling of hybrid frameworks. *Science* **315,** 1828–1831 (2007).

5. Lee, Y., Vogt, T., Hriljac, J. A., Parise, J. B. & Artioli, G. Pressure-induced volume expansion of zeolites in the natrolite family. *J. Am. Chem. Soc.* **124,** 5466–5475 (2002).
6. Goodwin, A. L., Keen, D. A. & Tucker, M. G. Large negative linear compressibility of $Ag_3[Co(CN)_6]$. *Proc. Natl Acad. Sci. USA* **105,** 18708–18713 (2008).
7. Chapman, K. W., Halder, G. J. & Chupas, P. J. Pressure-induced amorphization and porosity modification in a metal–organic framework. *J. Am. Chem. Soc.* **131,** 17546–17547 (2009).
8. Bennett, T. D. *et al.* Reversible pressure-induced amorphization of a zeolitic imidazolate framework (ZIF-4). *Chem. Commun.* **47,** 7983–7985 (2011).
9. Cairns, A. B., Thompson, A. L., Tucker, M. G., Haines, J. & Goodwin, A. L. Rational design of materials with extreme negative compressibility: selective soft-mode frustration in $KMn[Ag(CN)_2]_3$. *J. Am. Chem. Soc.* **134,** 4454–4456 (2011).
10. Cairns, A. B. *et al.* Giant negative linear compressibility in zinc dicyanoaurate. *Nature Mater.* **12,** 212–216 (2013).
11. Cai, W. & Katrusiak, A. Giant negative linear compression positively coupled to massive thermal expansion in a metal–organic framework. *Nature Commun.* **5,** 4337 (2014).
12. Cairns, A. B. & Goodwin, A. Negative linear compressibility. *Phys. Chem. Chem. Phys.* **17,** 20449–20465 (2015).
13. Goodwin, A. L. & Kepert, C. J. Negative thermal expansion and low-frequency modes in cyanide-bridged framework materials. *Phys. Rev. B* **71,** 140301 (2005).
14. Chapman, K. W. & Chupas, P. J. Pressure enhancement of negative thermal expansion behavior and induced framework softening in zinc cyanide. *J. Am. Chem. Soc.* **129,** 10090–10091 (2007).
15. Phillips, A. E., Goodwin, A. L., Halder, G. J., Southon, P. D. & Kepert, C. J. Nanoporosity and exceptional negative thermal expansion in single-network cadmium cyanide. *Angew. Chem. Int. Ed.* **47,** 1396–1399 (2008).
16. Liu, Y. *et al.* Reversible structural transition in MIL-53 with large temperature hysteresis. *J. Am. Chem. Soc.* **130,** 11813–11818 (2008).
17. Das, D., Jacobs, T. & Barbour, L. J. Exceptionally large positive and negative anisotropic thermal expansion of an organic crystalline material. *Nature Mater.* **9,** 36–39 (2010).
18. Duyker, S. G., Peterson, V. K., Kearley, G. J., Ramirez-Cuesta, A. J. & Kepert, C. J. Negative thermal expansion in $LnCo(CN)_6$ (Ln=La, Pr, Sm, Ho, Lu, Y): mechanisms and compositional trends. *Angew. Chem. Int. Ed.* **52,** 5266–5270 (2013).
19. Yao, Z.-S. *et al.* Molecular motor-driven abrupt anisotropic shape change in a single crystal of a Ni complex. *Nature Chem.* **6,** 1079–1083 (2014).
20. Fortes, A. D., Suard, E. & Knight, K. S. Negative linear compressibility and massive anisotropic thermal expansion in methanol monohydrate. *Science* **331,** 742–746 (2011).
21. Shepherd, H. J. *et al.* Antagonism between extreme negative linear compression and spin crossover in $[Fe(dpp)_2(NCS)_2]\cdot py$. *Angew. Chem. Int. Ed.* **51,** 3910–3914 (2012).
22. Cai, W., He, J., Li, W. & Katrusiak, A. Anomalous compression of a weakly CHO bonded nonlinear optical molecular crystal. *J. Mater. Chem. C* **2,** 6471–6476 (2014).
23. Pretsch, T., Chapman, K. W., Halder, G. J. & Kepert, C. J. Dehydration of the nanoporous coordination framework $Er^{III}[Co^{III}(CN)_6]\cdot 4(H_2O)$: single crystal to single crystal transformation and negative thermal expansion in $Er^{III}[Co^{III}(CN)_6]$. *Chem. Commun.* 1857–1859 (2006).
24. Kepert, D. L. *Inorganic Stereochemistry* (Springer-Verlag, 1982).
25. Kono, R. The dynamic bulk viscosity of polystyrene and polymethyl methacrylate. *J. Phys. Soc. Jpn* **15,** 718–725 (1960).
26. Neimark, A. V. *et al.* Structural transitions in MIL-53 (Cr): view from outside and inside. *Langmuir* **27,** 4734–4741 (2011).
27. Duyker, S. G. *et al.* Topotactic structural conversion and hydration-dependent thermal expansion in robust $LnM^{III}(CN)_6\cdot nH_2O$ and flexible $ALnFe^{II}(CN)_6\cdot nH_2O$ frameworks (A = Li, Na, K; Ln = La-Lu, Y; M = Co, Fe; $0 \leq n \leq 5$). *Chem. Sci.* **5,** 3409–3417 (2014).
28. Serra-Crespo, P. *et al.* Experimental evidence of negative linear compressibility in the MIL-53 metal–organic framework family. *CrystEngComm* **17,** 276–280 (2015).
29. Baughman, R. H., Stafström, S., Cui, C. & Dantas, S. O. Materials with negative compressibilities in one or more dimensions. *Science* **279,** 1522–1524 (1998).
30. Kunkely, H. & Vogler, A. Optical properties of $Gd^{III}[M^{III}(CN)_6]$ with M=Cr and Co. Phosphorescence from ligand-field states of $[M(CN)_6]^{3-}$ under ambient conditions. *Inorg. Chem. Commun.* **7,** 770–772 (2004).
31. Studer, A. J., Hagen, M. E. & Noakes, T. J. Wombat: the high-intensity powder diffractometer at the OPAL reactor. *Physica B* **385–386,** 1013–1015 (2006).
32. Brown, J. M. The NaCl pressure standard. *J. Appl. Phys.* **86,** 5801 (1999).
33. Besson, J. M. *et al.* Neutron powder diffraction above 10 GPa. *Physica B* **180,** 907–910 (1992).
34. Larson, A. C. & Von Dreele, R. B. *General Structure Analysis System (GSAS)*, Los Alamos National Laboratory Report LAUR 86-748 (Los Alamos National Laboratory, 2000).
35. Toby, B. H. EXPGUI, a graphical user interface for GSAS. *J. Appl. Crystallogr.* **34,** 210–213 (2001).
36. Cliffe, M. J. & Goodwin, A. L. PASCal: a principal axis strain calculator for thermal expansion and compressibility determination. *J. Appl. Crystallogr.* **45,** 1321–1329 (2012).
37. Kresse, G. & Furthmuller, J. Efficient iterative schemes for *ab initio* total-energy calculations using a plane-wave basis set. *Phys. Rev. B* **54,** 11169–11186 (1996).
38. Blöchl, P. E. Projector augmented-wave method. *Phys. Rev. B* **50,** 17953–17979 (1994).
39. Kresse, G. & Joubert, D. From ultrasoft pseudopotentials to the projector augmented-wave method. *Phys. Rev. B* **59,** 1758–1775 (1999).
40. Perdew, J. P., Burke, K. & Ernzerhof, M. Generalized gradient approximation made simple. *Phys. Rev. Lett.* **77,** 3865–3868 (1996).
41. Minisini, B., Hadj, L. E., Fomena, M. L., Garderen, N. V. & Tsobnang, F. A density functional study of the pressure induced phase transition in $LiYF_4$. *J. Phys. Condens. Matter* **18,** 2429 (2006).
42. Bouzid, A. *et al.* in *Molecular Dynamics Simulations of Disordered Materials* (eds Massobrio, C., Du, J., Bernasconi, M. & Salmon, P. S.) Ch. 12, 313–344 (Springer Series in Materials Science 215, Springer International, 2015).
43. Kearley, G. J., Johnson, M. R. & Tomkinson, J. Intermolecular interactions in solid benzene. *J. Chem. Phys.* **124,** 044514 (2006).
44. Grimme, S. Semiempirical GGA-type density functional constructed with a long-range dispersion correction. *J. Comput. Chem.* **27,** 1787–1799 (2006).
45. Delley, B. An all-electron numerical method for solving the local density functional for polyatomic molecules. *J. Chem. Phys.* **92,** 508–517 (1990).
46. Delley, B. From molecules to solids with the DMol3 approach. *J. Chem. Phys.* **113,** 7756–7764 (2000).

Acknowledgements

C.J.K. acknowledges financial support from the Australian Research Council. The neutron scattering experiments were performed under OPAL proposal P2455. The authors thank the Bragg Institute sample environment team for their assistance.

Author contributions

S.G.D., V.K.P. and C.J.K. conceived the study, analysed and interpreted the data, and wrote the paper. S.G.D., V.K.P., G.J.K. and A.J.S. performed the experiments and DFT calculations.

Additional information

Supplementary information is available in the online version of the paper. Reprints and permissions information is available online at www.nature.com/reprints. Correspondence and requests for materials should be addressed to V.K.P. and C.J.K.

Competing financial interests

The authors declare no competing financial interests.